J. Fluid Mech. (1979), *vol.* 92, *part* 4, *pp.* 671–690
Printed in Great Britain

Experiments on an aerofoil at high angle of incidence in longitudinal oscillations

By C. MARESCA, D. FAVIER AND J. REBONT
Institut de Mécanique des Fluides, Laboratoire Associé no. 3 du C.N.R.S., Marseille

(Received 1 December 1977 and in revised form 6 November 1978)

Details of flow visualization, aerodynamic forces and pitching moment, static pressure and skin friction measurements have been carried out on a symmetrical aerofoil at fixed angle of incidence in longitudinal oscillations parallel to the uniform airstream of a wind-tunnel.

This investigation shows weak unsteady effects at incidences below that of static stall. For higher incidences, strong unsteady effects appear and depend on the frequency and amplitude of the oscillations. The measurements indicate an overshoot of the instantaneous lift and drag which is explained by a strong vortex shedding process occurring during the dynamic stall encountered by the aerofoil in decelerated motion, as observed for profiles oscillating in pitch through stall. When the aerofoil is going forward in accelerated motion dynamic reattachment may be observed at very high incidence over a short part of the period of oscillation.

Dynamic stall and dynamic reattachment contribute to a favourable effect of unsteadiness on the mean lift coefficient, which increases as compared to the steady state one, and which is expressed through an empirical formula involving incidence, frequency and amplitude of oscillations. At given incidence, optimization of this feature is achieved by matching the frequency and the amplitude of oscillation, respectively with the frequency linked with the highest peak of energy in the wake, and with the distance between two consecutive vortices in the mean wake when modelled as a von Kármán's vortex street.

1. Introduction

Unsteady flows over lifting surfaces occur in a wide range of new aerodynamic problems. A few of the examples are the flows generated by devices such as turbomachines and helicopter rotors, which have received an upsurge of research activity in recent years. During the forward flight of a helicopter the flow past the rotor remains complex owing to three-dimensionality and unsteadiness. Relative to the individual blade-elements, the surrounding airstream varies periodically with large-amplitude fluctuations of velocity magnitude and chordwise incidence. However, the basic features of such an unsteady flow, can fundamentally be treated through two-dimensional models executing cyclic time-dependent motion. As suggested by McCroskey & Fisher (1972), the crossflow velocity component and the centrifugal effects due to blade rotation, can be neglected as far as unsteady stalling features are concerned. The complex aerodynamic behaviour of a blade section away from the tips,

0022-1120/79/4249-6910 $02.00

can be modelled through the simplified case of a two-dimensional aerofoil oscillating in pitch in an airstream of sinusoidally varying velocity.

Up to now, very few experimentalists have paid attention to the effects of oscillating airstreams over a stationary aerofoil at fixed incidence (see Pearce, Kunz & Malone 1976; Saxena, Fejer & Morkovin 1977). Most of the theoretical and experimental works in the field, are devoted to the particular case of an aerofoil oscillating in pitch around a mean incidence. Special considerations have been given to the so-called 'dynamic stall' occurring when the aerofoil operates at incidences higher than the static stall incidence. A recent paper of McCroskey (1977) summarizes some of the major investigations undertaken on this topic.

A rather different aspect in modelling the unsteady events occurring on rotor blade in forward flight, can be achieved by other types of time-dependent motion; such as harmonic motion of the aerofoil at fixed incidence, oscillating in translation parallel or normal to an undisturbed airstream.

In this work, experiments performed in a subsonic wind-tunnel in the case of a wing motion parallel to the uniform airstream are presented, for fixed incidences of the aerofoil (a NACA 0012) equal or larger than the incidence for maximum static lift. The investigations have been carried out by means of several measuring techniques suitable for unsteady flow analysis: torsion dynamometers (as described by Valensi & Rebont 1972), smoke-filaments visualization, pressure transducers and skin friction gauges at the surface of the aerofoil (see Rebont *et al.* 1977), and hot-wire anemometer probes.

Obviously, the concerned phenomena are closely linked with the reduced amplitude $\lambda = A\omega/V_\infty$ and the reduced frequency $k = c\omega/2V_\infty$, (where A and ω are respectively the amplitude and the rotational frequency of the oscillation, c the chord of the aerofoil and V_∞ the velocity of the undisturbed airstream). In the case of large incidences, the mechanism of dynamic reattachment of the boundary layer over part of the period, followed by a vortex shedding process is observed and analysed. Unsteady effect on the time histories of pressure and skin friction distributions, aerodynamic forces (lift, drag) and pitching-moment are also studied. An empirical formula concerning the averaged lift over a period is obtained as function of λ and k, for a wide range of angles of incidence below and above the angle of static stall. Optimization of the favourable unsteadiness effect on the mean lift coefficient is also discussed.

2. Experimental facilities and procedures

The tests were conducted in the I.M.F.M. low turbulence open circuit wind-tunnel. This tunnel has a test section of $0{\cdot}5 \times 1 \times 3$ m. Upstream of the nozzle seven high solidity screens reduce the free-stream turbulence level to about 0·2 %. The test section velocity, under steady flow conditions, can be varied from 2·5 to 20 m/s, so that the range of static Reynolds number $Re_c = V_\infty c/\nu$ is $5{\cdot}7 \times 10^4 \leqslant Re_c \leqslant 4 \times 10^5$.

The model consists in a rectangular wing (span $l = 0{\cdot}495$ m and chord $c = 0{\cdot}3$ m), with a NACA 0012 symmetrical profile of about 12° for angle of steady stall incidence. The aerofoil is held vertically in the test section by two masts through a gap on the wall, by which the supports are provided. These masts are supported by a suspension gear which allows angles of attack of $\pm 25°$ on the free-stream direction. The suspension gear is fixed on a frame oscillating sinusoidally in translation of

	From	to	Notations
Airstream velocity (m/s)	2·5	20	V_∞
Aerofoil incidence (deg)	$-25°$	25°	i
Oscillating amplitude (m)	0	0·17	A
Oscillating frequency (Hz)	0	5	f
Reynolds number/chord	$5{\cdot}7 \times 10^4$	4×10^5	Re_c
Reduced amplitude	0	1·20	λ
Reduced frequency	0	1·60	k
Ratio $\epsilon = \lambda/k = 2\,(A/c)$	0	1·13	ϵ

TABLE 1

amplitude A and rotational frequency $\omega = 2\pi f$, which can be obtained in the ranges $0 \leqslant A \leqslant 0{\cdot}17$ m and $0 \leqslant f \leqslant 5$ Hz. The flow conditions relative to tests conducted in this work, are summarized in table 1.

The wing can move freely in the test section as its span (0·495 m) is slightly smaller than the test section height (0·3 m). As the aspect ratio of the wing is about 8, no steady correction of end effects was done. The static pressure along the wall of the test section is very nearly equal to the outside atmospheric pressure, so that there is no flow through the gap provided on the wall to support the instrumented aerofoil.

The three-dimensional analytical corrections of data obtained for stalled aerofoils in oscillatory motion, is beyond the state of the art. However, it has been possible to partially ascertain the significance of the tunnel-wall boundary layer interference, and its effects on the flow direction. A directional X-hot wire anemometer probe, and a local pitot static probe, have been set-up two chord lengths ahead of the aerofoil mid-chord. The model was tested with and without end plates, and measurements of velocity and static pressure supplemented by smoke-filaments visualizations, were performed. Based on these above observations, it was determined that for dynamic tests, no wall correction had to be considered as significant, and that the flow was essentially two-dimensional as far as frequencies $k > 0{\cdot}11$ were concerned. Similar conclusions have already been raised in a recent experimental work by Carr, McAlister & McCroskey (1977), who proved the two-dimensional feature of the flow and the non significance of the wall effects, for a wing of NACA 0012 profile spanning the entire test section, and oscillating in pitch through stall for frequencies equal or above $k = 0{\cdot}15$. The geometrical dimension ratios used in this work and in the present study are closely similar (span-chord ratio of 1·66 in both cases, wind tunnel width-span ratio of 1·5 for Carr experiments and of 2 in our tests).

Although the static data flow are more dependent on wall corrections than the dynamic ones, they have not been corrected but used to non-dimensionalize the dynamic data flow. Thus the following results are referred to those of a static-flow aerofoil of high aspect ratio, which represents a suitable experimental tool to approach the ideal two-dimensional case. As the three-dimensional effects remain weak in our dynamic test for $k \simeq 0{\cdot}5$, the profile chord has been the only length-scale introduced.

Two torsion dynamometers dynamically calibrated have been used to measure the aerodynamic forces; one for the measurement of lift and drag, the other for the measurement of the aerodynamic moment at the quarter chord point of the aerofoil (see Valensi & Rebont 1972). Lift and drag are measured with the same dynamometer

by placing its axle respectively parallel or normal to the airstream direction. The measurements of forces and pitching-moment are thus not simultaneous.

Two other models of the same wing have been instrumented to perform surface pressure and skin friction distributions. Local static pressure was measured by 'Kulite' pressure transducers (CQH 125), fitted in containers and bonded to the aerofoil skin, with their ends aligned flush with the outside surface. The mid-span section of the wing, has been equipped with ten pressure transducers staggered along the centre-line on the upper side of the aerofoil. They were progressively spaced towards the trailing edge, including one at the leading edge (their chordwise co-ordinates were $x/c = 0, 0{\cdot}04, 0{\cdot}12, 0{\cdot}2, 0{\cdot}3, 0{\cdot}4, 0{\cdot}5, 0{\cdot}6, 0{\cdot}7, 0{\cdot}8$). The transducers which were of the strain-gage differential type, have been statically calibrated. Their high frequency response and insensibility to acceleration, were found to be reliable for measurement of unsteady pressure fluctuations (see Maresca, Rebont & Valensi 1975). Local skin friction measurements have been performed by means of nine hot-film gauges mounted flush with the aerofoil surface. Just like pressure transducers, the sensors were staggered so that the electrical leads of the upstream gauges cannot interfere with the downstream gauges. The chordwise positions of the sensors were similar to the pressure ones, except that there was no sensor at the leading edge because of the large profile curvature. The unsteady values τ of the skin friction were non-dimensionalized by the correlated steady ones τ_s, so that no quantitative calibration was required to evaluate the unsteadiness, assuming that the steady flow calibration was still valid in periodic flow. This assumption remains true as long as the movement frequency (< 5 Hz) is low, compared to the high frequency response of the gauge ($\simeq 10^6$ Hz).

As exemplified on the diagram of figure 1, all the measurements of forces, pitching-moment, static pressure and skin friction were digitized and stored by a 800-channels data acquisition system (Intertechnique Didac 800). The time history of the quantity G to be measured was performed at 200 different phases of a single period, and its mean value on 20 cycles of oscillations. The data were then harmonically analysed within a mini-computer (Hewlett Packard 9830 A) to yield the time-averaged value and the N Fourier harmonics in the following form:

$$\frac{G}{G_s} = C_0 + \sum_{n=1}^{N} C_n \cos(n\omega t + \phi_n),$$

where G_s is the static value, and C_0 is the time-averaged value of G/G_s over the period.

The synchronization is such that the top period origin corresponds to the maximum relative velocity of the model. This velocity is given by $V/V_\infty = 1 + \lambda \cos \omega t$, so that ϕ_n ($n = 1, 2, \ldots N$) represents the phase between the nth harmonic of G and the relative velocity of the model.

Various results were carried out on either the time history record or on the 20 cycles averaged-signal. During the first stage of the investigation, the N-terms harmonic analysis were performed on both instantaneous and averaged signals, for frequencies f varying in the range $1 \text{ Hz} \leqslant f \leqslant 4 \text{ Hz}$. It was found that for the first 4 harmonics the differences between the two signal results were small, and either of the two could be used to represent the original record. For the higher harmonics ($n \geqslant 5$), the amplitudes C_n got so small that they remained within the error band of

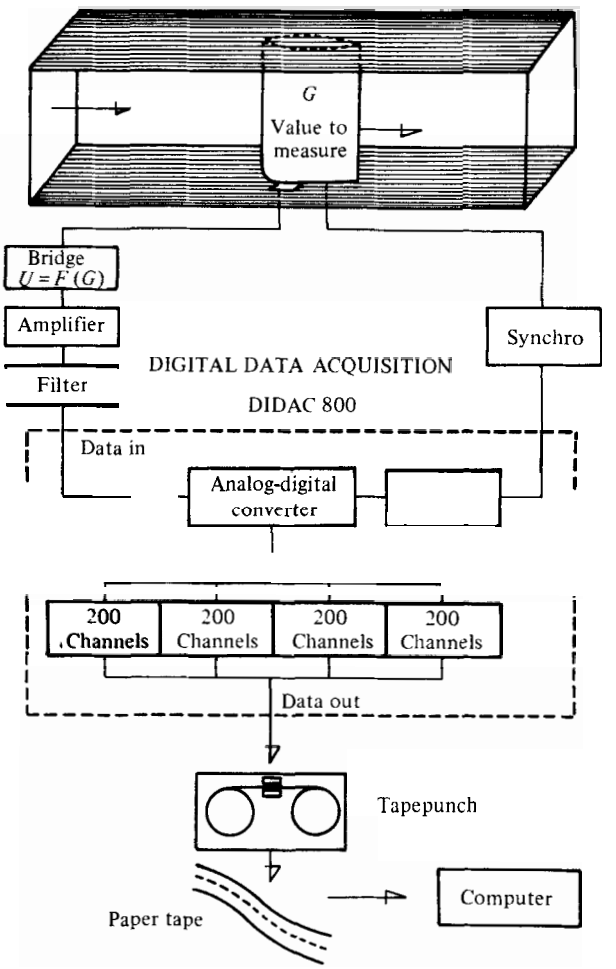

FIGURE 1. Block diagram of data acquisition.

the measuring technique, and the phase angles ϕ_n led to meaningless values. Therefore, only the first 4 harmonics of the Fourier series have been presented throughout the remainder of this study.

3. Results

3.1. *Mean overall aerodynamic forces and pitching-moment*

The dependence of the time-averaged overall forces and moment deduced from the torsion-dynamometers measurements on the flow parameters λ and k are presented in figures 2, 5 and 6 for angles of incidence varying from 0° to 20°. The figures, clearly demonstrate that the unsteady effects are weak at incidences below the angle of static stall i_{ss}, but get rapidly significant when λ and k parameters increase for incidences above i_{ss}.

Concerning the mean lift coefficient $C_{L0} = \bar{L}/\frac{1}{2}\rho V_\infty^2 cl$ where $\bar{L}$ is the average lift over the period, for instance figure 2 corresponding to $\lambda/k = \epsilon = 1{\cdot}13$, shows favourable unsteady effects as already pointed out by Rebont *et al.* (1975) and Maresca,

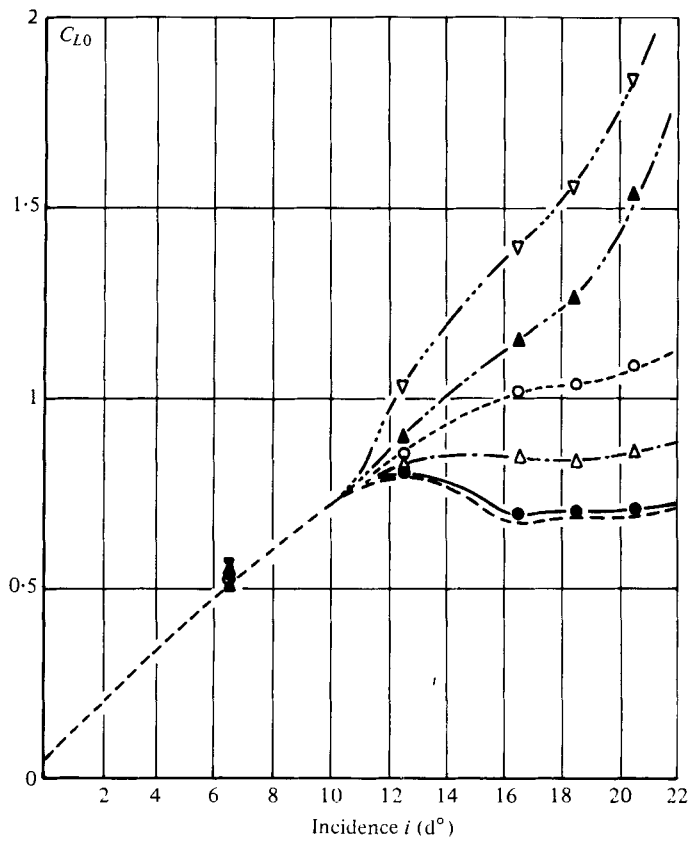

FIGURE 2. Variation with incidence of averaged lift coefficient $C_{L0} = \bar{L}/\frac{1}{2}\rho V_\infty^2 cl$; $A = 0{\cdot}17$ m; $f = 2{\cdot}5$ Hz; $A/c = 0{\cdot}565$; $\epsilon = 1{\cdot}13$. -----, steady values.

	—●—	-·-△-·-	---○---	-··-▲-··-	-···-▽-···-
λ	0·133	0·263	0·372	0·525	0·744
k	0·117	0·232	0·328	0·463	0·657
$Re_c \times 10^{-5}$	4·00	2·02	1·43	1·01	0·71

Rebont & Valensi (1976). A value of $C_{L0} \simeq 1{\cdot}75$ is obtained at an incidence of 20° and $\lambda = 0{\cdot}744$, whereas in steady conditions, for the same incidence, the lift coefficient is 0·7.

As increasing λ and k, significant effects due to unsteadiness can also be observed at high incidence on the time-averaged coefficients of drag C_{x0}, and moment C_{M0} (figures 5 and 6).

It is worthy to note that in the figures 3, 5, 6 discussed above, the amplitude ratio $A\omega/V_\infty$ and the reduced frequency $c\omega/2V_\infty$, were varied so that the ratio $\epsilon = \lambda/k$ keeps the same value ($\epsilon = 1{\cdot}13$) for all data plots. It is yet possible, from our experimental facilities, to separate the respective effects of each parameter λ and k. For example, by varying independently the amplitude A and the rotational frequency ω, while the velocity V_∞ remains constant. This has been done for wide ranges of A, λ, V_∞ and i as specified on table 1, and the output results have been fitted by various polynomial data fitting and least-squared methods. So, the mean lift – steady lift

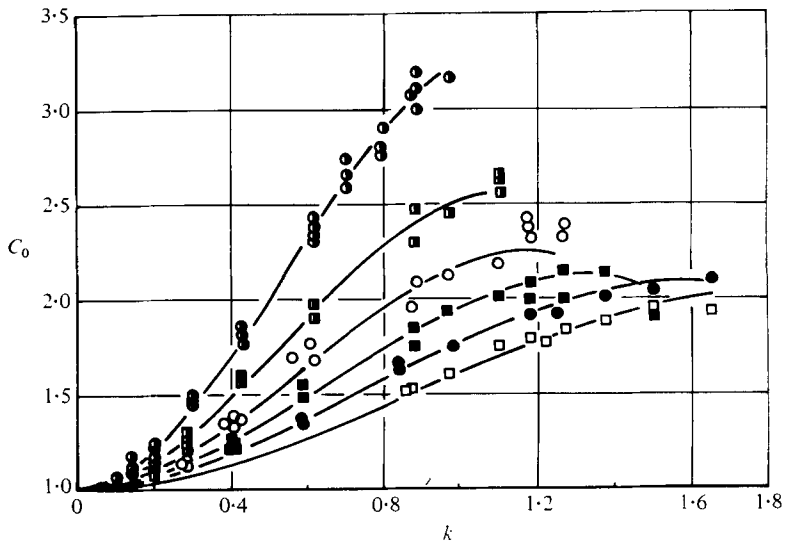

FIGURE 3. Variation with k of C_0 = (averaged lift $\bar{L}$)/(steady lift L_s) $i = 20°$; $0{\cdot}715 \times 10^5 < Re_c < 4 \times 10^5$. ——, equation (1). Experiments, ϵ values: ◑, 1·13; ◨, 0·79; ⊙, 0·55; ■, 0·39; ●, 0·27; □, 0·19.

ratio C_0, as defined above by G/G_s and obtained for the test conditions of table 1, has been synthetized by the following empirical formula:

$$C_0 = 1 + A(i)\,\epsilon^{\alpha} k^2 [1 - B(i)\,k(\epsilon)^{C(\epsilon)}], \tag{1}$$

$$\text{where: if } i \leqslant i_{ss} \left[A(i) = 0{\cdot}782 \left(\frac{i}{i_{ss}}\right); \alpha = 4; B(i) = 0{\cdot}2; C(\epsilon) = 5 \right.$$

and

$$\text{if } i \geqslant i_{ss} \left[\begin{array}{l} A(i) = 4 + 0{\cdot}6 \left(\dfrac{i}{i_{ss}}\right); \alpha = 1, \\ B(i) = 0{\cdot}558 + 0{\cdot}432 \left| 2{\cdot}17 - \left(\dfrac{i}{i_{ss}}\right) \right|^3; \\ C(\epsilon) = 0{\cdot}422 - 055\epsilon. \end{array} \right.$$

As a few example, figure 3 shows for $i = 20°$, the experimental values of C_0 *versus* k for several values of ϵ. For each value of ϵ, equation (1) has been represented by dash line.

In the range of mean Reynolds number explored ($5{\cdot}7 \times 10^4 \leqslant Re_c \leqslant 4 \times 10^5$), the static data have shown little influence with Re_c either at 6° or 20°. The dynamic data time-averaged over a period and presented in figure 3 have been non-dimensionalized by the steady value measured at Reynolds number based on the mean value of the velocity during the cycle. A same value of k can be reached by varying the values of V_∞ and ω in such a way that ω/V_∞ is kept constant. The gathering of data (figure 3) obtained at fixed ϵ and k for several V_∞ and ω shows that, even if the dynamic results could be influenced by the variation of Reynolds number during the cycle, the parameter k keeps a universal character and is well representative of the observed phenomenon at least in the range $5{\cdot}7 \times 10^4 \leqslant Re_c \leqslant 4 \times 10^5$.

Moreover, the data show that C_0 presents a maximum value with varying k, at fixed ϵ. When ϵ is increased, the maximum of C_0 is obtained for decreasing values of k. The continuous increase of C_0 with ϵ at fixed k can also be mentioned.

A calculation of k and ϵ leading to maximum value of C_0, can be attempted by considering the mechanism of vortex shedding occurring when the model oscillates at a frequency f. In first approximation, we may assume that the stalled wing has an aerodynamic behaviour similar to that of a flat plate, set at an incidence i in an airstream of velocity V_∞. At $Re_c \simeq 10^5$, the vortex shedding of the flat plate in steady airstream induces a frequency spectrum in the wake with a peak of energy located at f_m corresponding to a Strouhal number:

$$St = \frac{f_m h}{V_s} = 0{\cdot}16 \tag{2}$$

as shown by Roshko (1955); h is the width of the wake and V_s the velocity of free-streamline at separation. Moreover, if we assume that the wing in unsteady motion has an equivalent mean wake of width h and oscillates at frequency f_m, it may be expected that the frequency of vortex generation matches with the frequency of the peak of energy in the wake. The reduced frequency k_m may then be written:

$$k_m = \pi c f_m / V_\infty.$$

At $i = 20°$, the velocity of free-streamline of a flat plate wake can be given by $V_s = 1{\cdot}3\, V_\infty$ (see Comolet, 1976). Under these conditions we obtain:

$$k_m = 0{\cdot}653 c/h. \tag{3}$$

If we assume now that the coupling between the vortex shedding and the wake structure is perfect, the two vortices shedded in the wake during one oscillation will be distant of d in such a manner that $d = 2A$ (see figure 4). The Kármán's stability ratio $h/d = 0{\cdot}28$ gives $h/2A = 0{\cdot}28$. At the optimum exchange of energy between the movement of the model and the wake, the ratio $\epsilon = \lambda/k = 2A/c$ may be written:

$$\epsilon_M = h/0{\cdot}28c. \tag{4}$$

In the case of small unsteady effect corresponding to low values of λ, h can be approximated by the expression $h = 1{\cdot}41\, c \sin i$, which assumes that the width of the mean wake has the same value that in steady case (see Comolet 1976); for $i = 20°$, k_M and ϵ_M become

$$k_M = 1{\cdot}36 \quad \text{and} \quad \epsilon_M = 1{\cdot}72. \tag{5}$$

At higher values of λ and k, it is possible to give an expression of h/c by use of the drag coefficient C_D. The equation (11) proposed in the paper of Roshko (1955) leads to

$$h/c \simeq 1{\cdot}7\, C_D \quad \text{in the case of} \quad i = 20°.$$

Introducing this value in equations (5), we obtain:

$$k_M = 0{\cdot}51/C_D \quad \text{and} \quad \epsilon_M = 6{\cdot}4\, C_D. \tag{6}$$

The equations (6) confirm the previously mentioned fact that k_M decreases when ϵ increases. Moreover for values of ϵ not very large, the experimental values of k_M (see figure 3) are in good agreement with the approximated values of equation (5). Unfortunately, our experimental facilities do not allow to reach values of ϵ larger than 1·13.

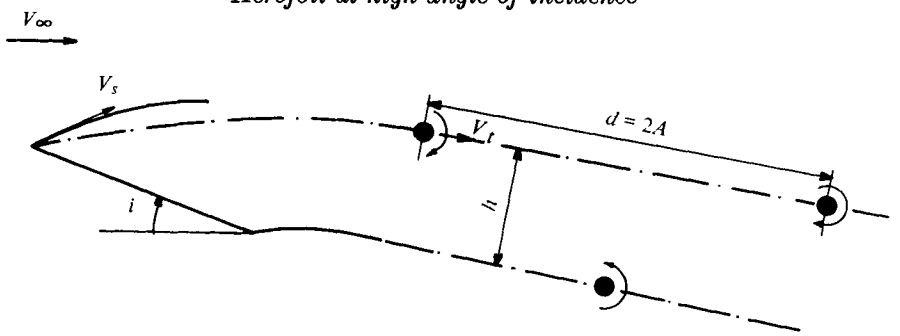

FIGURE 4. Vortex shedding pattern of a flat plate.

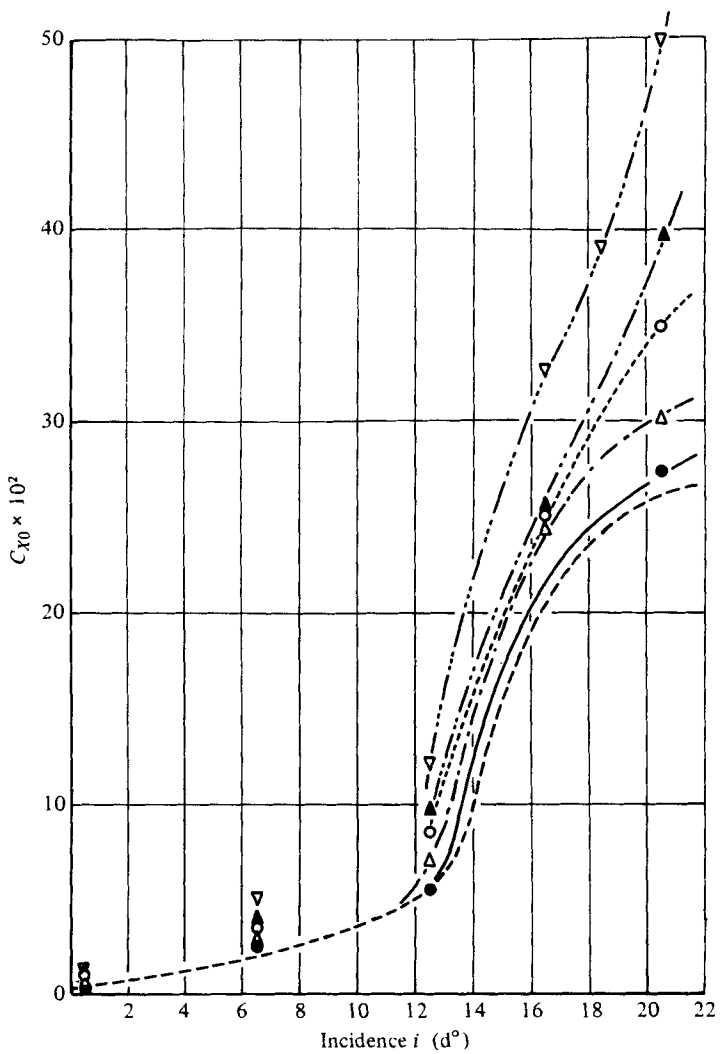

FIGURE 5. Variation with i of averaged drag coefficient $C_{X0} = \bar{D}/\frac{1}{2}\rho V_\infty^2 cl$; $A = 0{\cdot}17$ m; $f = 2{\cdot}5$ Hz; $A/c = 0{\cdot}565$; $\epsilon = 1{\cdot}13$. -----, steady values; symbols as in figure 2.

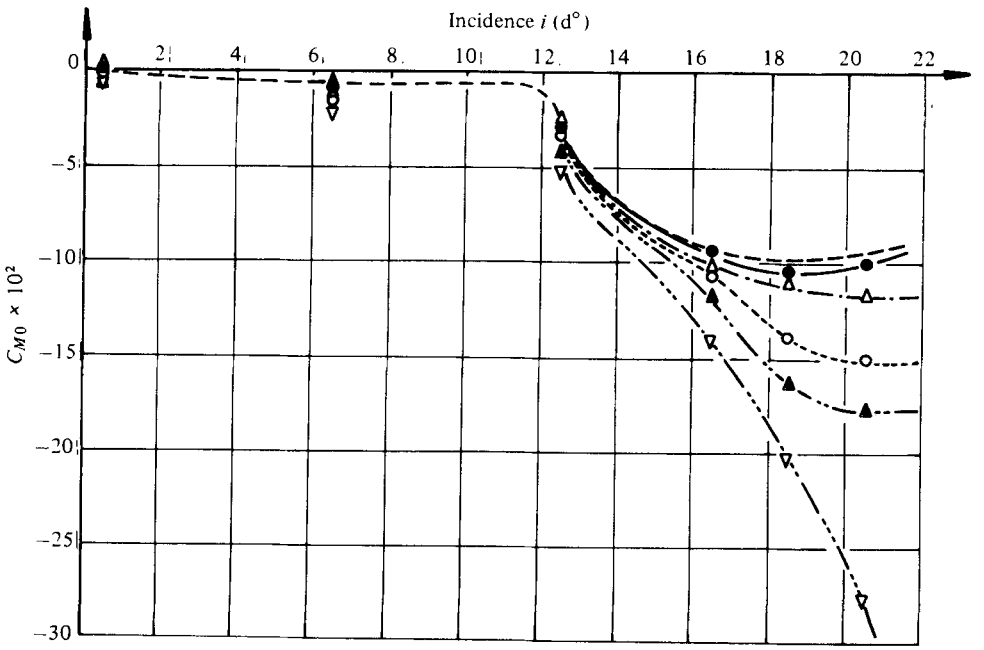

FIGURE 6. Variation with i of averaged moment coefficient $C_{M_0} = \bar{M}/\frac{1}{2}\rho V_\infty^2 c^2 l$. $A = 0{\cdot}17$ m; $f = 2{\cdot}5$ Hz; $A/c = 0{\cdot}565$; $\epsilon = 1{\cdot}13$. -----, steady values; symbols as in figure 2.

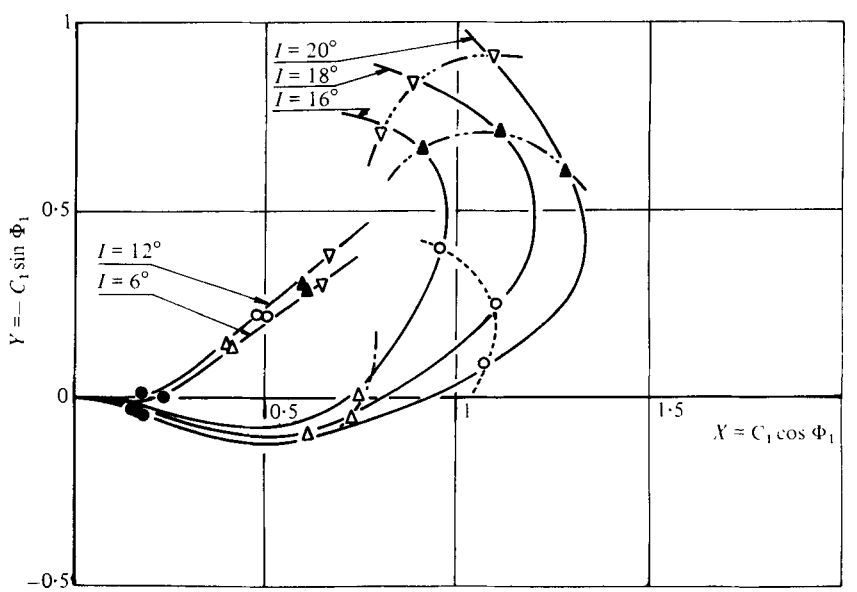

FIGURE 7. Variation with i of first harmonic (C_1, ϕ_1) of $L_{(i)}/L_s$ = unsteady lift/steady lift. $A = 0{\cdot}17$ m; $f = 2{\cdot}5$ Hz; $A/c = 0{\cdot}565$; $\epsilon = 1{\cdot}13$. Symbols as in figure 2.

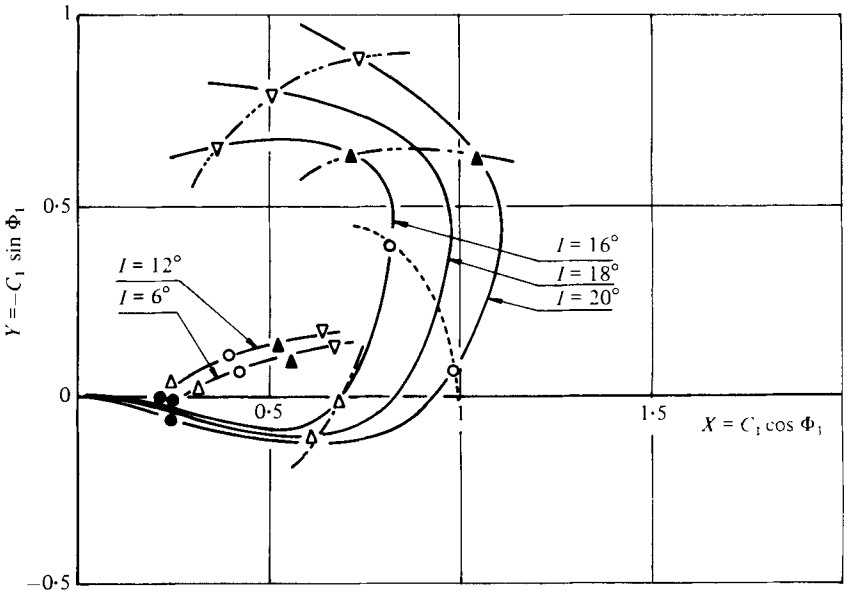

FIGURE 8. Variation with i of first harmonic (C_1, ϕ_1) of $D_{(t)}/D_s$ = unsteady drag/steady drag. Symbols as in figure 2.

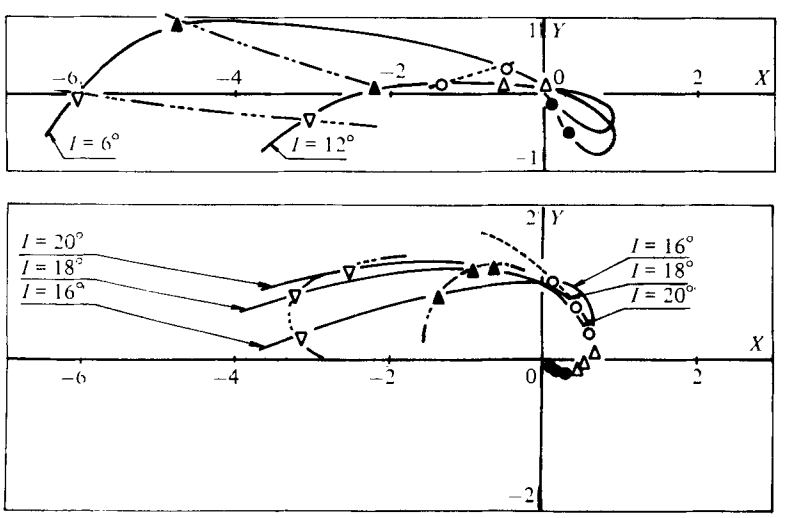

FIGURE 9. Variation with i of first harmonic (C_1, ϕ_1) $M_{(t)}/M_s$ = unsteady moment/steady moment. $A = 0{\cdot}17$; $f = 2{\cdot}5$ Hz; $A/c = 0{\cdot}565$; $\epsilon = 1{\cdot}13$. Symbols as in figure 2.

Thus, the unsteady effects produced by the oscillation of the wing induce an overshoot of the mean lift coefficient which can be optimized by a phenomenon 'like resonance' between the vortex shedding and the movement of the wing. This lift coefficient-gain is however coupled with a drag and moment coefficients increase as seen in figures 5 and 6 (relative to $\epsilon = 1{\cdot}13$). At angles of attack above i_{ss}, the dynamic data indicate averaged wake-widths and nose-down moments larger than the steady ones, as λ increases from 0 to 0·74.

3.2. *Fourier analysis of the overall aerodynamic forces*

The results obtained in the ranges of A, V_∞, ω and i summed up in table 1 were explicited in Fourier series of 4th order.

As an example, and for respectively the lift L, the drag D and the aerodynamic moment M, figures 7, 8, 9 present the dependence of the 1st harmonic phase-angle ϕ_1 and amplitude C_1 (plotted in the diagram $C_1 \cos\phi_1, -C_1 \sin\phi_1$), on i and λ at $\epsilon = 1{\cdot}13$. As long as the incidence is below i_{ss}, it can be seen that the phase angle ϕ_1 keeps a constant value of about 40° concerning L (figure 7), and 30° concerning D (figure 8); the amplitude C_1 growing with increasing λ.

As soon as the incidence is above i_{ss}, ϕ_1 goes back to zero at very low values of λ, then grows with increasing λ and i; whereas C_1 presents a maximum value which increases with incidence and occurs at phase angle decreasing with increasing incidence (see figures 7 and 8).

When ϵ is varied, the display of data keeps a similar behaviour to those described above, however the maximum value of C_1 decreases with ϵ and ϕ_1 seems to present a constant value when $i < i_{ss}$.

Regarding the variation of ϕ_1 and C_1 for the aerodynamic moment (figure 9), strong changes in ϕ_1 and C_1 may be observed ($0 \leqslant \phi_1 \leqslant 360°$ and $0 < |C_1| < 7$) when ϵ is decreased from 1·13 to 0·19.

The data showed additionally that the amplitudes of second harmonic C_2 for L, D and M have values well below C_1 although ϕ_2 may become very large. The amplitudes of the 3rd and 4th harmonic are so small that they can be neglected. So, only two harmonics are sufficient to give a good approximation and thus the real values of L, D and M are well approximated by considering two harmonics only.

The influence of λ, k and i can also be assessed by considering the non-dimensional values of L, D and M (based on the static values) as functions of time. The quasi-steady expression for these quantities which may be written as

$$(L/L_s)_{qs} = (D/D_s)_{qs} = (M/M_s)_{qs} = (1 + \lambda \cos \omega t)^2 \tag{7}$$

have been compared to the instantaneous ones. We will later discuss in details the time-history of the aerodynamic forces, in particular case of $i = 20°$, $\lambda = 0{\cdot}74$, $\epsilon = 1{\cdot}13$, $Re_c = 0{\cdot}714 \times 10^5$. However, it may be already said that on the one hand unsteady values obtained at low λ and k ($\lambda < 0{\cdot}26$ and $k < 0{\cdot}23$) check very well the quasi-steady equation (7), i.e. unsteady effects are not globally appreciable in this case. On the other hand, as soon as λ and k are respectively above 0·26 and 0·23, unsteady effects become strong particularly when the incidence is above i_{ss}. One of the main features of these effects is an increase of the mean lift compared to the static value as discussed in a preceding section. This increase is confirmed by pressure measurements performed on the model. Indeed the mean lift given by integration of the mean pressure coefficient $\overline{C_{p(t)}}$ plot of figure 10 obtained at $i = 20°$, $\lambda = 0{\cdot}744$, $k = 0{\cdot}657$, would be about 2·1 times higher than the mean lift given by the static pressure coefficient C_{ps} data plotted on the same figure. This value is in good agreement with the result of torsion dynamometer measurement (see figure 3). However the data of figure 11, relative to $i = 6°$, $\lambda = 0{\cdot}744$ and $k = 0{\cdot}657$, lead to a mean lift increase $\bar{L}/L_s$ of 1·15, revealing weak unsteady effects as expected at low incidence.

As illustrated in figures 5 and 6, unsteady effects lead to high value of mean drag

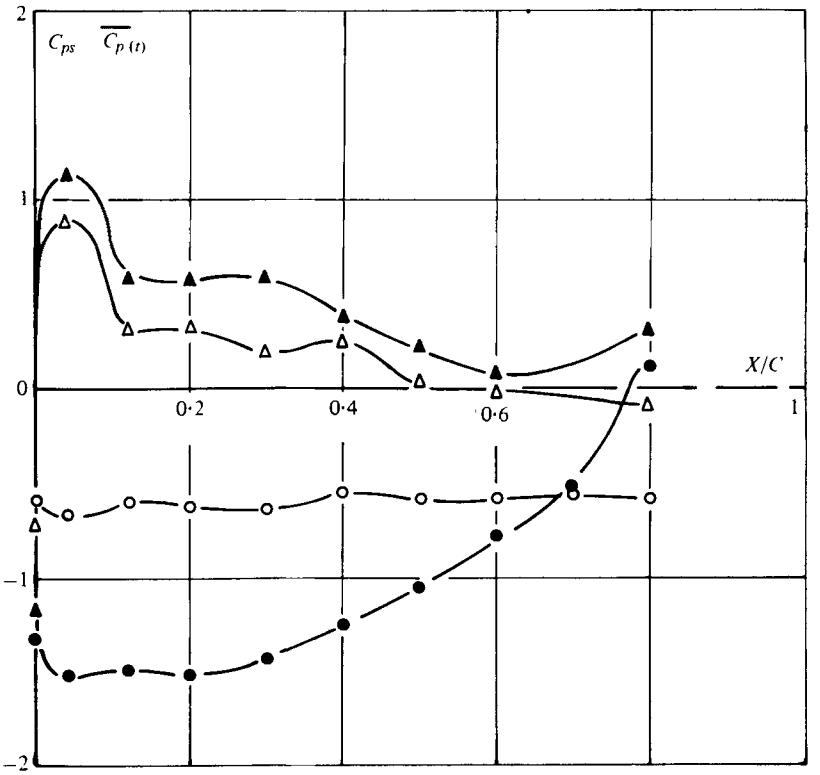

FIGURE 10. Distribution of averaged $\overline{C_{p(t)}}$ and steady C_{ps} pressure coefficient. $i = 20°$; $A = 0{\cdot}17$ m; $f = 2{\cdot}5$ Hz; $A/c = 0{\cdot}565$; $\epsilon = 1{\cdot}13$; $Re_c = 0{\cdot}714 \times 10^5$; $\lambda = 0{\cdot}744$; $k = 0{\cdot}657$. Upper surface: ○, steady; ●, average value. Lower surface: △, steady; ▲, average value.

and nose-down moment. Concerning the drag, the mean skin friction $\overline{\tau_{(t)}}$ non-dimensionalized by static skin friction τ_s has been plotted in figure 12 at incidences of 6° and 20°. It can be seen that on the lower side where the distribution of $\overline{\tau_{(t)}}/\tau_s$ is flat with a value of about 1, (except at $x/c = 0{\cdot}7$ where the transition of the boundary layer may occur at 6° incidence) the unsteady effects are very weak. On the contrary, the data for the upper surface indicate strong unsteady effects characterized by two peaks located at mid-chord and at $x/c \simeq 0{\cdot}2$.

3.3. *Visualization and discussion of the instantaneous phenomena*

The series of photographs of figure 13 (plate 1) taken at an exposure of 1/1000 s at different phases of the period, describe the anatomy of the flow field over the upper surface of the wing in the following conditions: $i = 20°$, $\lambda = 0{\cdot}74$, $\epsilon = 1{\cdot}13$,

$$Re_c = 0{\cdot}71 \times 10^5.$$

The steady state flow is shown in the bottom right-hand picture. The flow patterns on the other photographs indicate that the flow is reattached at $\omega t = 1{\cdot}76\pi$, whereas at $\omega t = 1{\cdot}9\pi$ a leading edge bubble grows ($\omega t = 0{\cdot}2\pi$) and bursts ($0{\cdot}3\pi$, $0{\cdot}4\pi$). The wake is then larger ($\omega t = 1{\cdot}4\pi$) than the steady one. The left-hand part of figure 13 presents, from top to bottom, position, relative velocity and acceleration of the model corresponding to the phases of photographs shown in the figure.

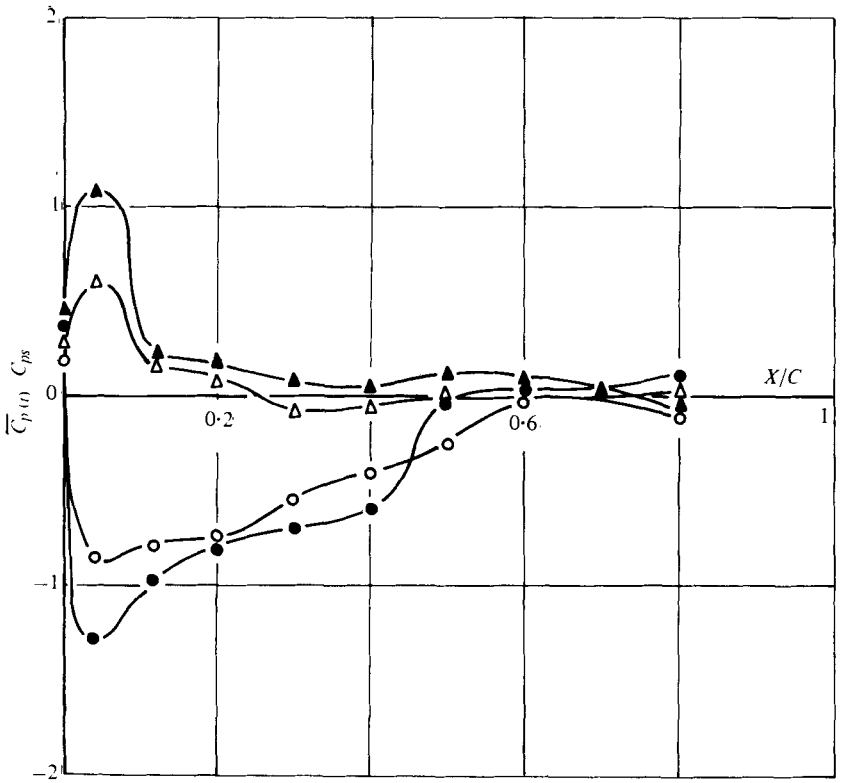

FIGURE 11. Distribution of averaged $\overline{C_{p(t)}}$ and steady C_{ps} pressure coefficient. Same conditions as figure 10 but $i = 6°$.

A film realized with the aid of a fast running camera operated at 300 frames/s gave clearly the evolution with time of the different flow patterns encountered during a period. In the case described above, the 'dynamic reattachment' is observed for only a short part of the period, when the aerofoil is going forward in accelerated motion. Rolling vortices from leading edge to trailing edge are also present on the upper surface and are shed in the wake when the bubble is bursting.

The unsteady values of forces and pitching-moment (L/L_S, D/D_S, M/M_S) of C_p and τ/τ_s may be discussed in the light of the corresponding flow pictures. This is done for five phase angles typical of the main features of the flow ($\frac{3}{2}\pi$; $1{\cdot}76\pi$; $1{\cdot}9\pi$; $0{\cdot}2\pi$; $0{\cdot}74\pi$).

(*a*) $\omega t = \frac{3}{2}\pi$. The photograph obtained at $\omega t = \frac{3}{2}\pi$ compared to the steady state photograph (figure 14, plate 2) reveals that the flow is partially reattached on the upper surface. At this time the model is ready to move upstream ($v/V_\infty = 1$); the acceleration reaches its maximum value $A\omega^2$. It can be seen in figure 14(*a*) that the lift, drag and pitching-moment have values very near the quasi-steady ones, which in this case are also the steady values. The unsteady pressure coefficient C_p defined by $C_p = (p - p_\infty)/\frac{1}{2}\rho V_\infty^2$ is compared to C_{pS} in figure 14(*b*). It can be seen that a suction region occurs on the upper surface significative of a reattachment of the flow as confirmed by the visualization.

The measurements of τ/τ_s plotted in figure 14(*c*) show that the skin friction is higher than the steady one on the whole upper surface. This may be explained by the reattachment of the flow.

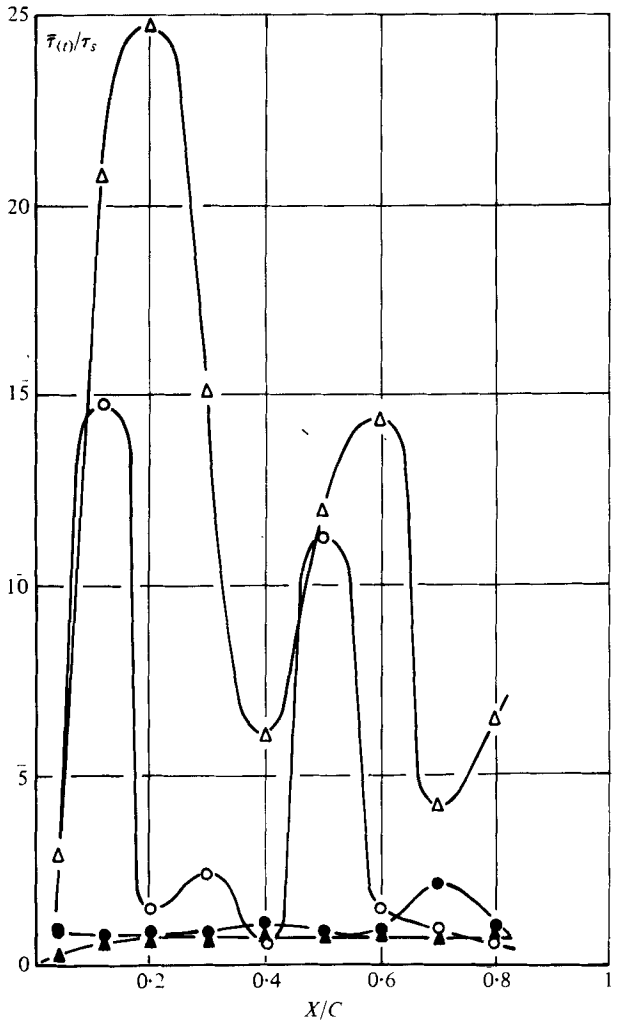

FIGURE 12. Averaged skin friction $\bar{\tau}/\tau_s$ distribution. $A = 0{\cdot}17$ m; $f = 2{\cdot}5$ Hz; $A/c = 0{\cdot}565$; $\epsilon = 1{\cdot}13$; $Re_c = 0{\cdot}714 \times 10^5$; $\lambda = 0{\cdot}744$; $k = 0{\cdot}657$. $i = 6°$; ○, upper surface; ●, lower surface. $i = 20°$: △, upper surface; ▲, lower surface.

(*b*) $\frac{3}{2}\pi \leqslant \omega t \leqslant 1{\cdot}9\pi$. The aerofoil is going forward and the relative velocity is accelerated. The flow becomes attached over the whole upper surface as shown in figure 15 (plate 3) where $v/V_\infty = 1{\cdot}56$. The lift is higher than the quasi-steady value, the drag lower, and the pitching moment becomes nose up. The reattachment of the flow is corroborated by the pressure and skin friction distributions (right-hand side of figure 15), which show the presence of a suction region with high skin friction on the upper surface. It may be noticed that on the lower surface the values of the skin friction are nearly equal to the steady ones.

(*c*) $1{\cdot}9\pi \leqslant \omega t \leqslant 0{\cdot}3\pi + 2\pi$. The picture of figure 16 (plate 4) reveals a bubble extending from the leading edge to midchord, whereas reverse flow seems to appear from trailing edge to midchord.

At this time, the velocity of the aerofoil is $1{\cdot}7\,V_\infty$ and the acceleration is about $0{\cdot}3\,A\omega^2$. The lift, the drag and the pitching-moment keep on growing. A suction region and high skin friction may be observed on the upper surface.

In figure 17 (plate 5) corresponding to $\omega t = 0{\cdot}2\pi$, $v/V_\infty = 1{\cdot}6$, the photograph indicates that a vortex is progressing from leading edge to trailing edge just after the burst of the bubble. The lift and the drag have values well above the quasi-steady ones, and the two strong peaks which appear in the skin friction distribution may be due to vortices.

As soon as $0{\cdot}2\pi \leqslant \omega t \leqslant 0{\cdot}3\pi$, lift and drag reach their maxima. At $\omega t = 0{\cdot}3\pi$ the pitching-moment has a first maximum.

(*d*) $0{\cdot}3\pi \leqslant \omega t \leqslant \frac{3}{2}\pi$. In this zone, lift and drag are decreasing and reach the steady value at $\omega t = \frac{3}{2}\pi$ ($v/V_\infty = 1$).

At $\omega t = 0{\cdot}74\pi$, the photograph of figure 18 (plate 6) where $v/V_\infty = 0{\cdot}49$ shows that the flow is separated on the whole upper surface and the resulting wake is larger than the steady wake. The second maximum of the pitching moment obtained at $\omega t = \pi$ may be explained by the shedding of vortices from the trailing edge.

Relative to the rolling vortex phenomenon mentioned in (*c*), the time-histories of static pressure and skin friction were carried out at different stations of the surface. Upper surface waveforms of instantaneous static pressure from $x/c = 0$ to $x/c = 0{\cdot}8$, at $i = 20°$, $\lambda = 0{\cdot}74$; $\epsilon = 1{\cdot}13$ and $Re_c = 0{\cdot}71 \times 10^5$ are illustrated in figure 19 for two periods.

The pressure at $x/c = 0{\cdot}12$ reaches a minimum at $\omega t = 1{\cdot}9\pi$ indicating that the vortex has been shed and is rolling downstream, as confirmed by successive minima suction peaks at locations from $x/c = 0{\cdot}1$ to $x/c = 0{\cdot}8$. The vortex moves at about 43 % of the relative velocity corresponding to $\omega t \simeq 2\pi$.

Figure 20 gives the upper surface waveforms of instantaneous skin friction from $x/c = 0{\cdot}04$ to $0{\cdot}8$ obtained at $i = 20°$, $\lambda = 0{\cdot}74$, $\epsilon = 1{\cdot}13$ and $Re_c = 0{\cdot}71 \times 10^5$ during two periods. The skin friction at $x/c = 0{\cdot}12$ presents a maximum which occurs at nearly the same time that the suction peak at $x/c = 0{\cdot}12$ of figure 19. The successive maxima at locations aft of $x/c = 0{\cdot}12$ show the moving downstream vortex at velocity whose value agrees with the velocity calculated by use of waveforms pressure.

Figure 21 shows the lower surface waveforms of instantaneous skin friction, at the same experimental conditions that figure 20. It may be observed that no skin friction peak occurs, the variation of skin friction during the period being only dependent on the relative velocity whereas the boundary layer remains laminar.

The above phenomenological results are in good agreement with phenomena observed in the case of aerofoils oscillating in pitch (see McCroskey 1977).

In both cases, the vortex shedding process induces lift and drag overshoot and maximum negative moment during dynamic stall. The maximum lift is reached when the vortex is approximately at midchord. The maximum diving moment occurs as soon as the vortex core passes off the trailing edge. Then the aerofoil enters full stall, and a new maximum negative moment is observed whereas lift and drag decrease to values more representative of static stall. This second maximum negative moment can be attributed to a second vortex like disturbance which forms ahead of midchord and moves downstream. Therefore we can notice that the dynamic stall events of aerofoils oscillating in pitch or in longitudinal oscillations parallel to the undisturbed stream are quite similar.

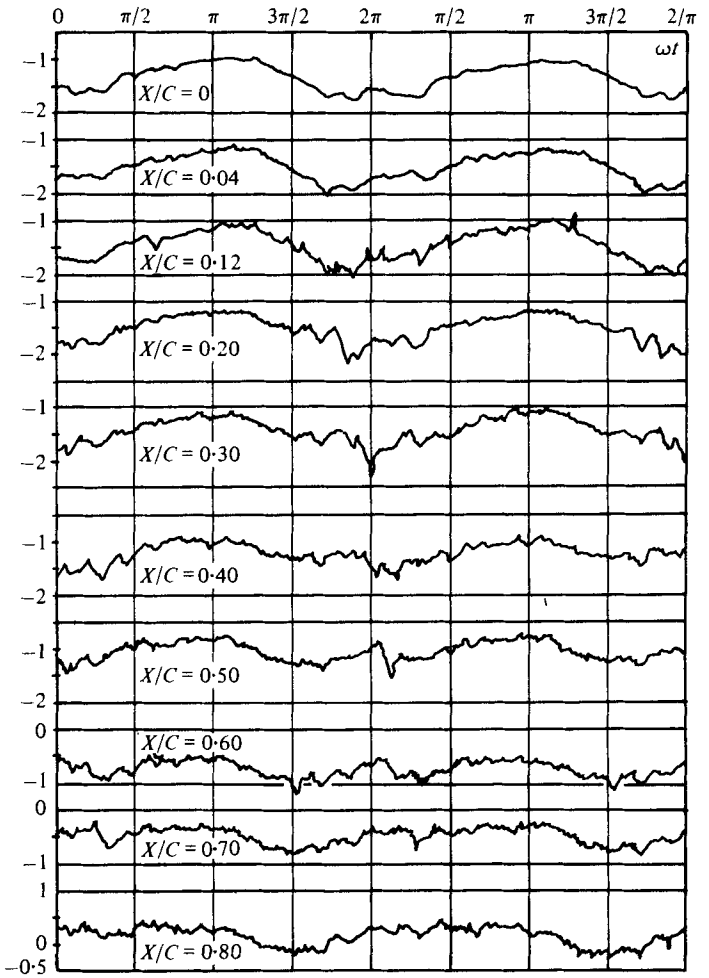

FIGURE 19. Waveforms of static pressure on the upper surface.
$i = 20°$; $\lambda = 0{\cdot}74$; $Re_c = 0{\cdot}714 \times 10^6$; $A = 0{\cdot}17$ m; $f = 2{\cdot}5$ Hz.

Concerning the flow reattachment, in both cases the boundary layer flow reattaches to the aerofoil progressively from the leading edge. However, when the aerofoil is oscillated in pitch, reattachment only occurs when the aerofoil enters incidences well below angle of static stall (say 6° when $i_{ss} = 12°$). In the case of oscillations parallel to undisturbed flow, the reattachment is obtained during a part of the period, at an incidence well above i_{ss} (say 20°). This reattached boundary layer flow is a purely unsteady phenomenon; indeed during the period the aerofoil never encounters quasi-steady situations for which the boundary layer is reattached, and then cannot remember this event as it is the case in oscillations in pitch.

4. Conclusions

Based on the qualitative and quantitative results presented above, the following features of the flow over an aerofoil in longitudinal oscillations parallel to the undisturbed airstream can be pointed out.

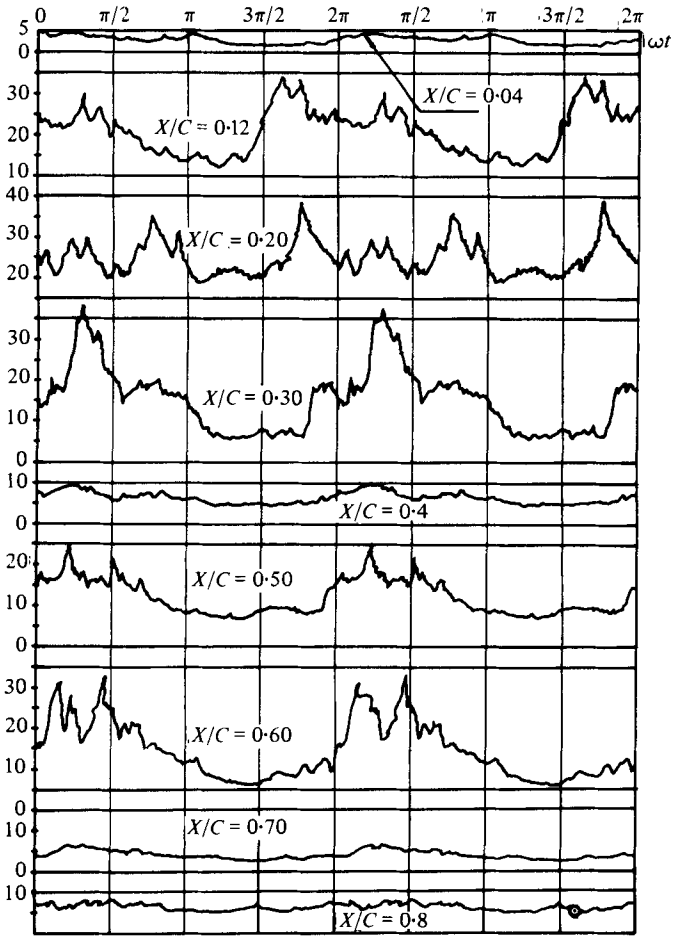

FIGURE 20. Waveforms of skin friction on the upper surface. Same conditions as figure 19.

At incidences below the angle of static stall, unsteady effects are weak and slightly affected by the frequency and amplitude of oscillation. At incidences above the angle of static stall, the unsteady effects are dependent on incidence, frequency and amplitude of oscillation.

Averaged results showed favourable effects of unsteadiness on the lift coefficient. Mean lift overshoot could be given by an empirical formula; optimal values of frequency and amplitude leading to maximum value of this mean lift overshoot may be predicted, assuming a mean ideal wake pattern as a von Kármán's vortex street in which the frequency of the peak of energy matches with the frequency of oscillation. However it must be said that large mean drag and nose-down pitching-moment are also obtained, indicating averaged wake widths larger than the steady case ones.

Instantaneous data reveal that the oscillating airfoil was experiencing both dynamic stall, and dynamic reattachment. Dynamic stall is initiated by a large bubble which bursts, giving rise to vortex shedding characterized by a vortex rolling from the leading edge to the trailing edge. This vortex shedding process induces instantaneous

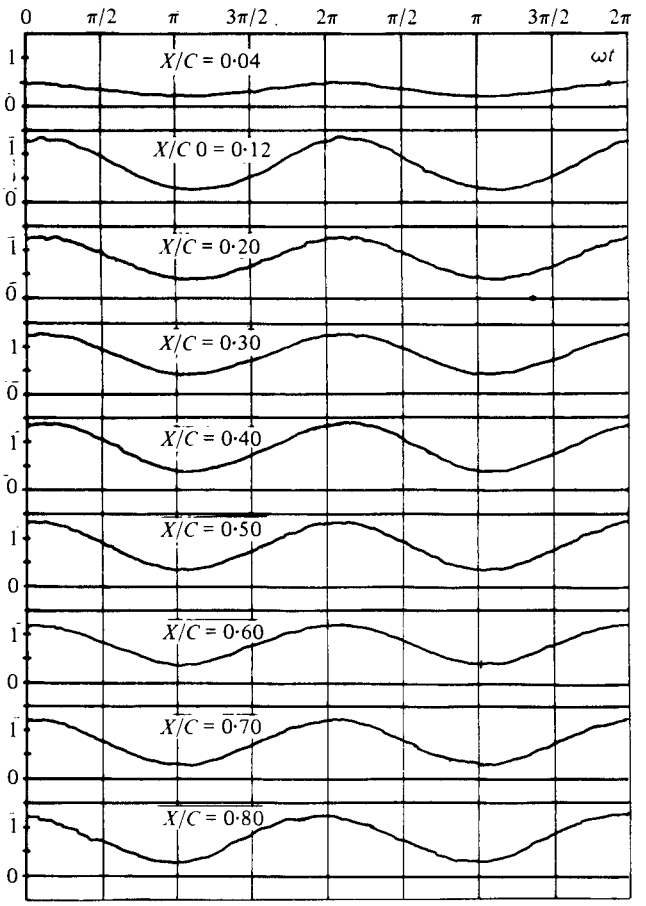

FIGURE 21. Waveforms of skin friction on the lower surface.
Same conditions as figure 20.

lift and drag overshoot and maximum diving moment. These events are quite similar to that observed in the case of oscillations in pitch (see McCroskey 1977).

Dynamic reattachment which occurs progressively from the leading edge may be observed at very high incidence (20°) for a short part of the period, when the aerofoil is going forward in accelerated motion. The mechanism by which the flow reattaches at so large incidence is one of the unsolved problems in the analysis of dynamic reattachment, as the formation of the vortex in the mechanism of vortex shedding is an unsolved problem in the analysis of dynamic stall.

Finally, we have obtained a certain amount of information about the phenomenology of an aerofoil in unsteady motion. It now remains to study the unsolved afore mentioned problems, and it is hoped that the availability of data will increase in the future and will lead to a satisfying theoretical model involving dynamic separation and reattachment.

This work was supported by Service Technique Aeronautique Contract no. 76-98214-00481-7586.

REFERENCES

CARR, L. W., MCALISTER, K. W. & MCCROSKEY, W. J. 1977 Analysis of the development of dynamic stall based on oscillating airfoil experiments. *N.A.S.A. Tech.* Note D-8382.

COMOLET, R. 1976 *Dynamique des Fluides Réels* (2nd edition, ed. Masson), p. 227.

MCCROSKEY, W. J. & FISHER, R. K. 1972 Detailed aerodynamic measurements on a model rotor in the blade stall regime. *J. Amer. Hel. Soc.* **17**, 1, 20.

MCCROSKEY, W. J. 1977 Some current research in unsteady fluid dynamics. The 1976 Freeman Scholar Lecture. *Trans. A.S.M.E. J. Fluids Engng.* **99**, 8.

MARESCA, C., REBONT, J. & VALENSI, J. 1975 Separation on reattachment of the boundary layer on a symmetrical aerofoil oscillating at fixed incidence in a steady flow. In *Proc. Univ. Arizona/USAF OSR Symp. Unsteady Aerodynamics* (ed. R. B. Kinney), vol. 1, p. 35.

MARESCA, C., REBONT, J. & VALENSI, J. 1976 Caractéristiques aérodynamiques d'un profil en mouvement instationnaire. In *IUTAM 14th Int. Cong. Theor. Appl. Mech., Delft.* Springer.

PIERCE, G. A., KUNZ, D. L. & MALONE, J. B. 1976 The effect of varying freestream velocity on dynamic stall characteristics. In *32nd Ann. Nat. V/Stol Forum Amer. Hel. Soc. Washington D.C.*

REBONT, J., MARESCA, C., GUILERMINET, A. & FAVIER, D. 1975 Etude expérimentale relative à l'aérodynamique d'un rotor d'hélicoptère en vol de translation. In *Proc. 12ième Coll. Aérodyn. Appl. ENSMA CEAT, Poitiers.*

REBONT, J., MARESCA, C., FAVIER, D. & VALENSI, J. 1977 Recollement dynamique sur un profil d'aile en mouvement de tamis. Influence des paramètres d'oscillation. In *Proc. AGARD-FDP Meeting Unsteady Aerodyn., Ottawa.*

ROSHKO, A. 1955 On the wake and drag of bluff bodies. *J. Aero. Soc.* **22**, 2, 124.

SAXENA, L. S., FEJER, A. A. & MORKOVIN, M. V. 1977 Features of unsteady flow over airfoils. In *Proc. AGARD-FDP Meeting Unsteady Aerodyn., Ottawa.*

VALENSI, J. & REBONT, J. 1972 Efforts aérodynamiques sur un profil d'aile animé d'un mouvement harmonique parallèle à l'écoulement. In *Proc. AGARD-FDP Meeting Aérodyn. Rotary Wing, Marseille.*

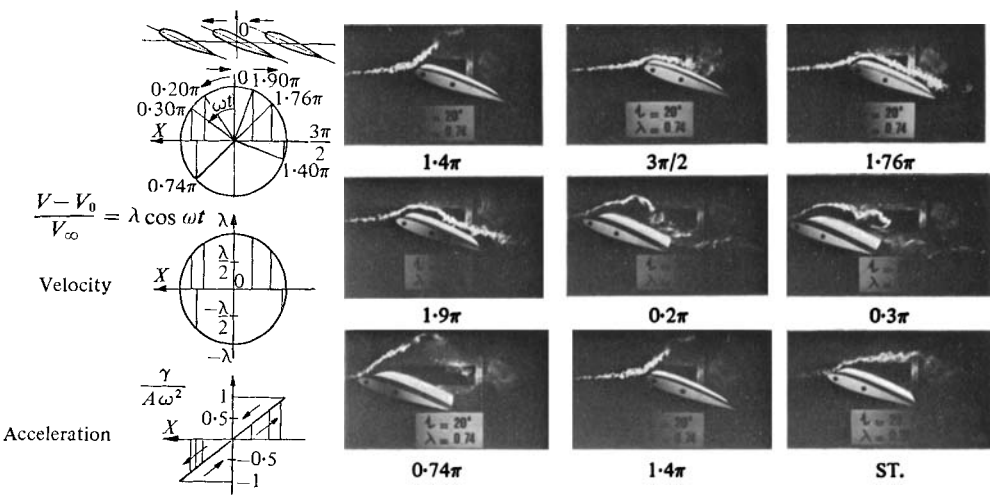

FIGURE 13. Flow visualization by smoke filaments.
$A = 0{\cdot}17$ m; $f = 2{\cdot}5$ Hz; $Re_c = 0{\cdot}714 \times 10^5$; $\epsilon = 1{\cdot}13$.

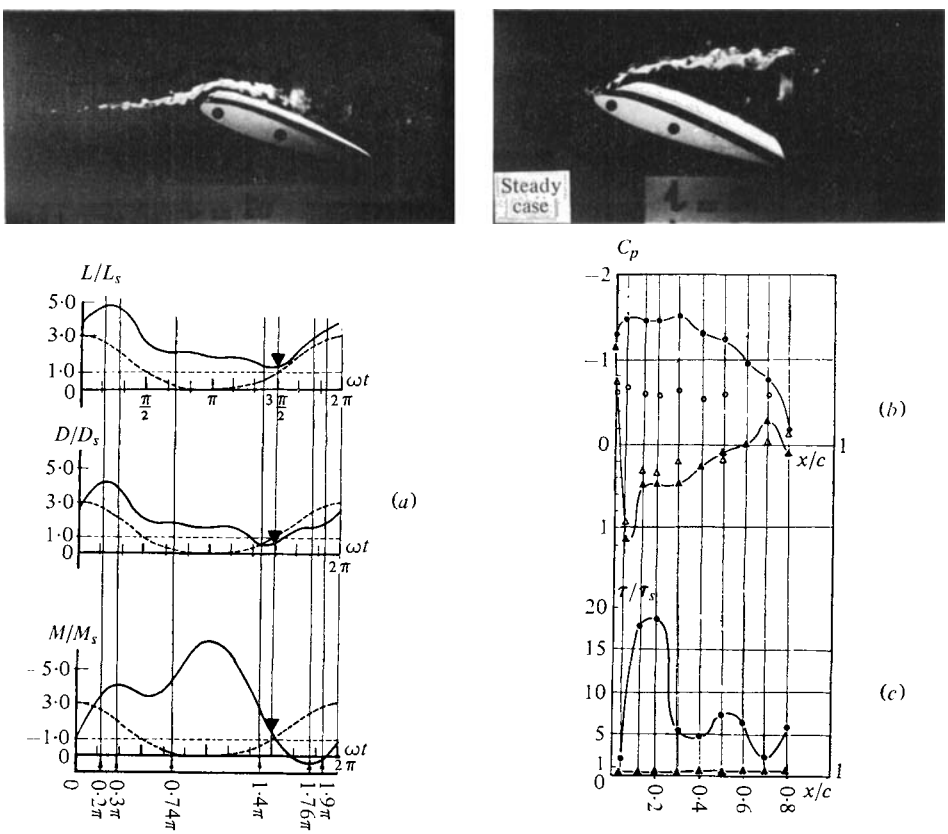

FIGURE 14. Instantaneous phenomena: $\omega t = \frac{3}{2}\pi$, $v/V_\infty = 1$, $i = 20°$; $\lambda = 0{\cdot}74$; $\epsilon = 1{\cdot}13$; $Re_c = 0{\cdot}714 \times 10^5$; $A = 0{\cdot}17$ m; $f = 2{\cdot}5$ Hz. (*a*) Experimental instantaneous lift, drag, moment; ———, quasi-steady values. (*b*) Pressure coefficient. Upper surface: ●, Unsteady; ○, steady; Lower surface: ▲, unsteady; △, steady. (*c*) Skin friction τ/τ_s: ●, upper surface; ▲, lower surface.

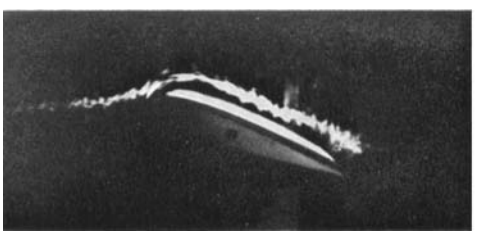

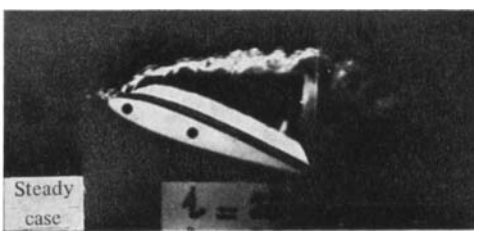

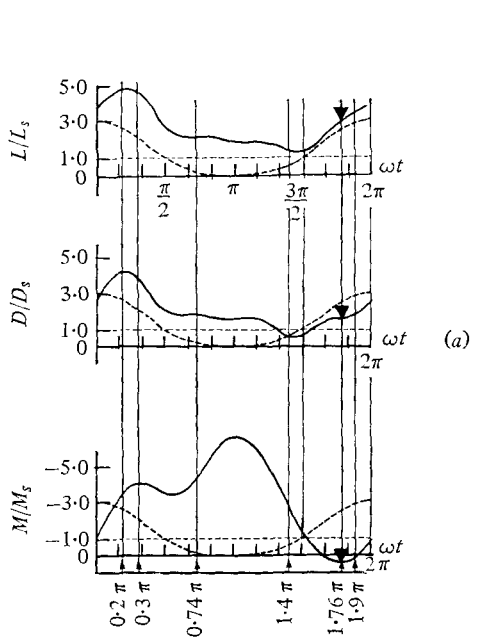

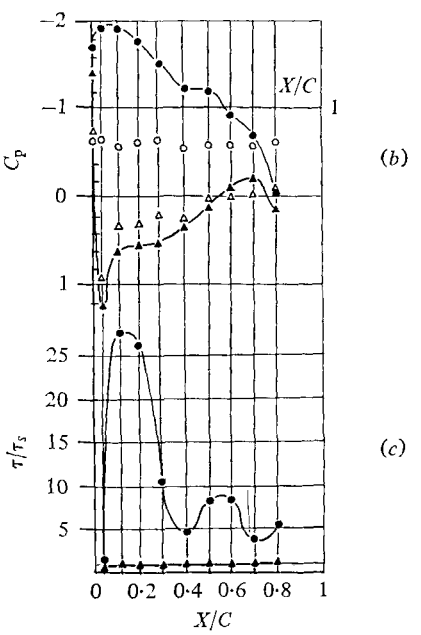

FIGURE 15. Instantaneous phenomena; $\omega t = 1{\cdot}76\pi$; $v/V_\infty = 1{\cdot}56$; same conditions as figure 14.

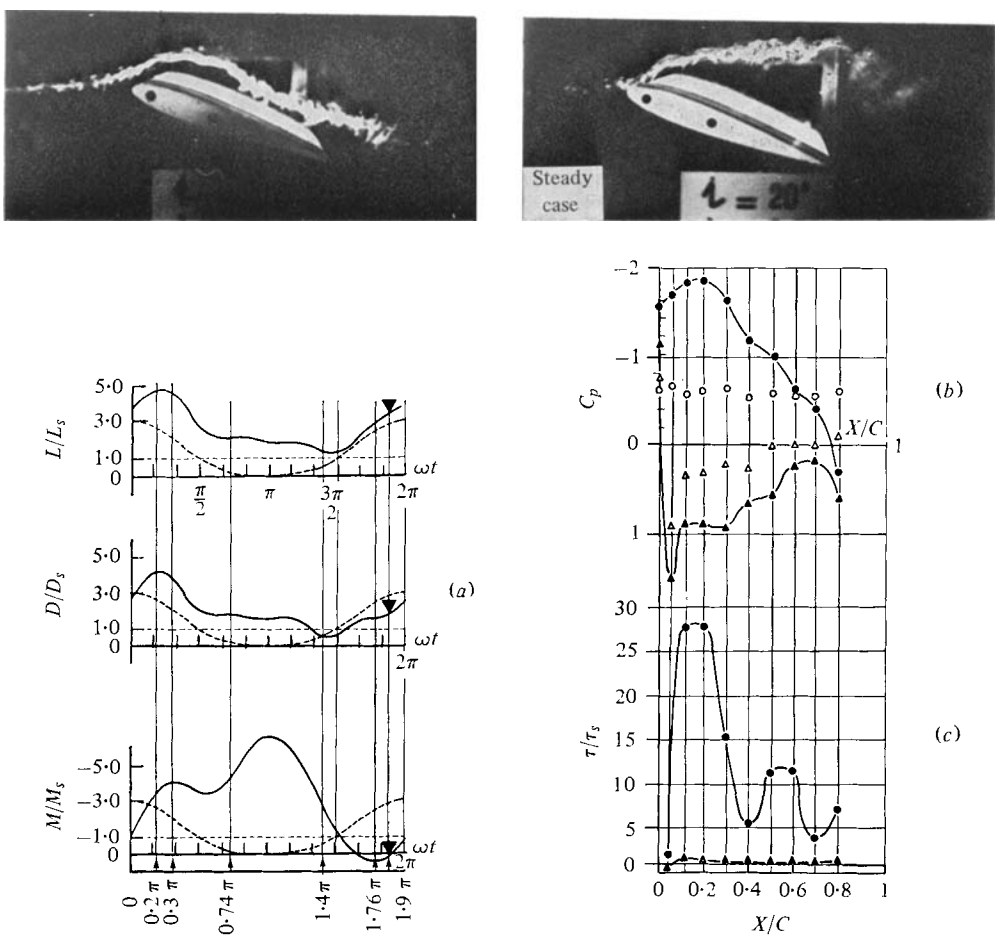

FIGURE 16. Instantaneous phenomena: $\omega t = 1{\cdot}9\pi$; $v/V_\infty = 1{\cdot}7$.
Same conditions as figure 14.

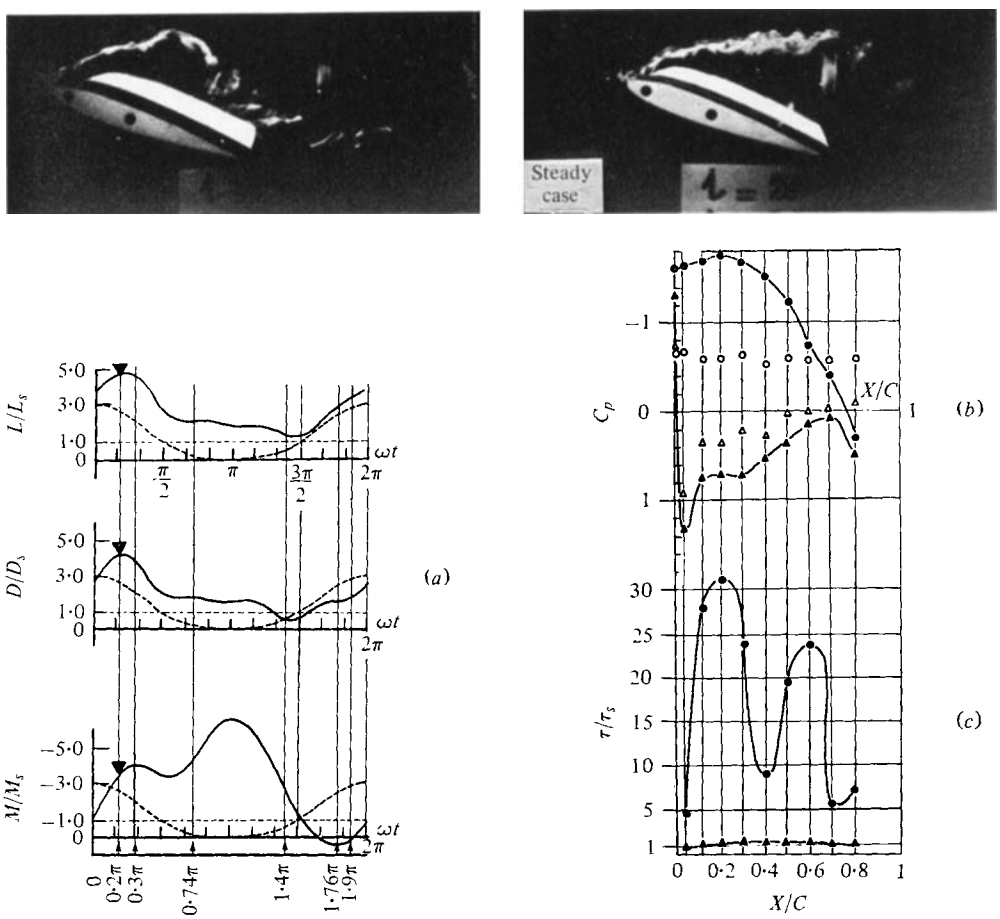

FIGURE 17. Instantaneous phenomena: $\omega t = 0{\cdot}20\pi$; $v/V_\infty = 1{\cdot}6$.
Same conditions as figure 14.

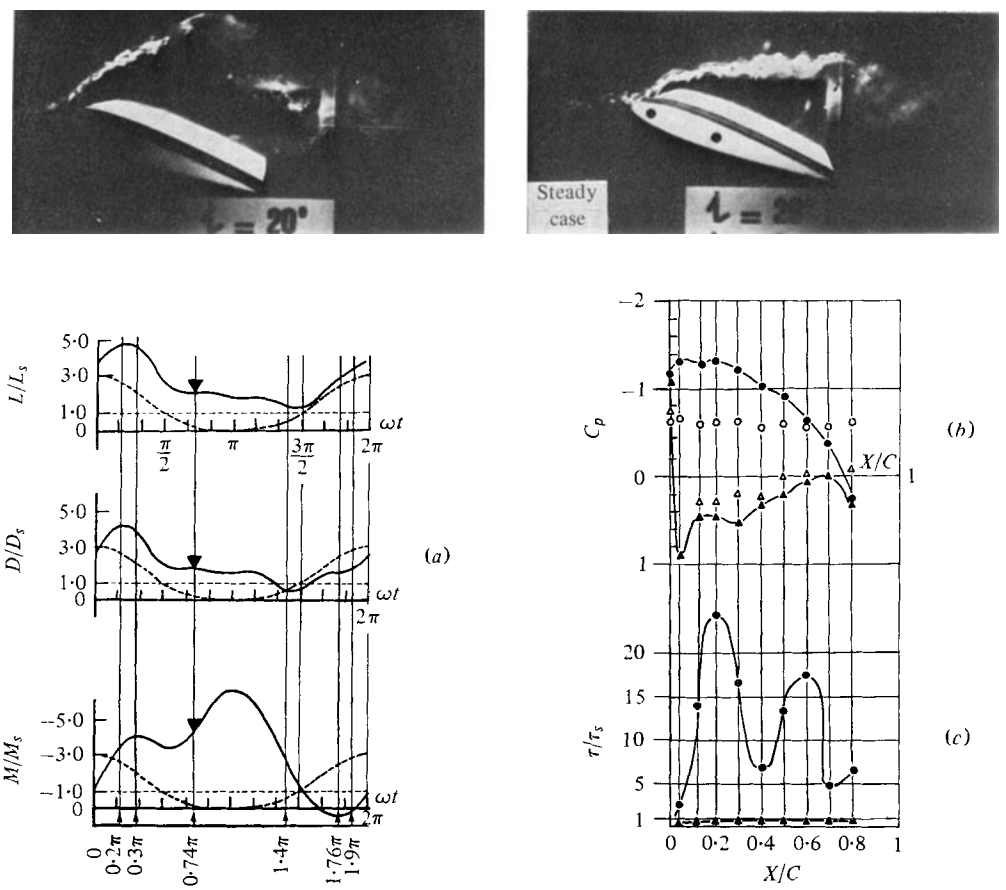

FIGURE 18. Instantaneous phenomena: $\omega t = 0{\cdot}74\pi$; $v/V_\infty = 0{\cdot}49$.
Same conditions as figure 14.